molecules

MDPI

Article

Customizing Pore System in a Microporous Metal–Organic Framework for Efficient C_2H_2 Separation from CO_2 and C_2H_4

Qiang Zhang †, Guan-Nan Han †, Xin Lian, Shan-Qing Yang and Tong-Liang Hu *

School of Materials Science and Engineering, National Institute for Advanced Materials, Nankai University, Tianjin 300350, China

* Correspondence: tlhu@nankai.edu.cn (T.-L.H.)

† These authors contributed equally to this work.

Abstract: Selective-adsorption separation is an energy-efficient technology for the capture of acetylene (C_2H_2) from carbon dioxide (CO_2) and ethylene (C_2H_4). However, it remains a critical challenge to effectively recognize C_2H_2 among CO_2 and C_2H_4, owing to their analogous molecule sizes and physical properties. Herein, we report a new microporous metal–organic framework (**NUM-14**) possessing a carefully tailored pore system containing moderate pore size and nitro-functionalized channel surface for efficient separation of C_2H_2 from CO_2 and C_2H_4. The activated **NUM-14** (namely **NUM-14a**) exhibits sufficient pore space to acquire excellent C_2H_2 loading capacity (4.44 mmol g^{-1}) under ambient conditions. In addition, it possesses dense nitro groups, acting as hydrogen bond acceptors, to selectively identify C_2H_2 molecules rather than CO_2 and C_2H_4. The breakthrough experiments demonstrate the good actual separation ability of **NUM-14a** for C_2H_2/CO_2 and C_2H_2/C_2H_4 mixtures. Furthermore, Grand Canonical Monte Carlo simulations indicate that the pore surface of the **NUM-14a** has a stronger affinity to preferentially bind C_2H_2 over CO_2 and C_2H_4 via stronger C-H···O hydrogen bond interactions. This article provides some insights into customizing pore systems with desirable pore sizes and modifying groups in terms of MOF materials toward the capture of C_2H_2 from CO_2 and C_2H_4 to promote the development of more MOF materials with excellent properties for gas adsorption and separation.

Keywords: metal–organic frameworks; moderate pore size; hydrogen bond receptor; C_2H_2/CO_2 separation; C_2H_4 purification

Citation: Zhang, Q.; Han, G.-N.; Lian, X.; Yang, S.-Q.; Hu, T.-L. Customizing Pore System in a Microporous Metal–Organic Framework for Efficient C_2H_2 Separation from CO_2 and C_2H_4. *Molecules* **2022**, *27*, 5929. https://doi.org/10.3390/molecules27185929

Academic Editors: Yun-Lei Peng and Ying Zhang

Received: 18 August 2022
Accepted: 8 September 2022
Published: 12 September 2022

1. Introduction

Accompanied by worldwide economic advances, energy demand and supply have appeared cumulatively prominent; the thirst for high-purity raw materials, conveniently feasible technological streams, and desired final products has turned into even more unprecedented impendency. Industrial chemical separations occupy a large proportion of the quotient of global energy consumption, which has achieved a spectacular 10–15%, amounting to half of the usage amount of industrial energy in the United States [1]. Among the multitudinous commodity chemicals involving industrial interest, acetylene (C_2H_2) and ethylene (C_2H_4) are the two kinds of the most critical feedstocks for the electronic industry and polymerization manufacturing. Mature C_2H_2 fabrication methods in the petrochemical industry mainly rely on thermal cracking of hydrocarbons or partial oxidation of natural gas, and then obtained C_2H_2 production can be employed to cut/weld metals or manufacture diversiform high-value chemicals, such as vinyl chloride, acetaldehyde, acrylic acid derivatives, and synthetic fiber/rubber [2]. However, carbon dioxide (CO_2) as an unwished impurity is inevitably mingled in the obtained C_2H_2 production during the aforementioned preparation processes, which will ultimately injure the quality of the downstream chemical products [3]. Therefore, the separation of C_2H_2/CO_2 mixtures became of great importance in the petrochemical industry. In addition, C_2H_4, as an indispensable building block in

the chemical synthesis industry with global annual production about 201 Mt by 2020, is generally used to manufacture polyethylene, vinyl chloride, ethylene oxide, etc. [4]. C_2H_4 is usually obtained by the catalytic cracking of hydrocarbons and steam cracking of naphtha; nevertheless, trace amounts of C_2H_2 as contaminants often inevitably coexist in C_2H_4 production. These C_2H_2 impurities about 1000–5000 ppm not only would significantly affect the quality of the resulting polyethylene but also can further form solid metal acetylide to block the fluid stream-triggering explosion [5]. Under this background, capturing trace C_2H_2 from C_2H_2/C_2H_4 mixture to purify C_2H_4 also became an imperative task. The similar geometric characteristics, including molecular size and shape, and alike physical properties mainly referring to the boiling point between C_2H_2 and CO_2 or C_2H_4 molecules, render the separations of C_2H_2/CO_2 and C_2H_2/C_2H_4 mixtures as high-challenge scientific problems [6–8]. Researchers in the petrochemical industry have devoted massive efforts to pursuing solutions for overcoming these separation difficulties. The current commercial pathway principally depends on cryogenic distillation, which has a high energy penalty and expensive economic cost. Porous materials utilizing selective physisorption with high energy efficiency, low investment cost, and environmentally friendly peculiarity might provide a promising alternative to separate these troublesome mixtures.

Metal–organic frameworks (MOFs) with large surface area, high porosity, fascinating modularity, and abundant functionality, as new-style crystalline porous materials, are constructed with metal ions/clusters and organic linkers. Because of their unique characteristics, MOFs have received wide attention in numerous application fields, such as gas storage and separation, heterogeneous catalysis, proton conduction, and fluorescence detection [9–12]. The most remarkable advantage of MOF materials over other traditional porous materials (such as zeolite, silica gel, and porous carbon) lies in the tunability of the pore system, predominantly referring to pore size/shape and pore surface chemistry. Plentiful adsorption-based MOFs were explored to address C_2H_2 separations challenges, which have obtained certain achievements [13,14]. Although a large number of research results indicated that incorporating strong binding sites (such as Lewis basic sites and open metal sites) into large-pore MOFs can effectively promote high C_2H_2 uptake capacities, most of them exhibited low separation selectivity and even terrible actual dynamic breakthrough properties due to their large pore size [15,16]. On the other side, the introduction of fluorinated anions (such as SiF_6^{2-}, $NbOF_5^{2-}$, and TiF_6^{2-}) as hydrogen-bonding acceptors (HBAs) into ultra-microporous pillared hybrid MOFs can preferentially bind C_2H_2 molecules to dramatically enhance the separation selectivity [17,18]. However, the majority of ultra-microporous MOFs with excellent separation performance exhibited relatively low C_2H_2 loading capacity owing to their limited pore space. Recently, through the structure–performance relationship screening of 62 reported top-performing C_2H_2 adsorbents, Zhai et al. found that tuning the aperture of MOFs within the range of moderate pore size (5.0–7.5 Å), combined with accessible HBAs, is an effective route to break through the trade-off barrier between C_2H_2 storage and C_2H_2/CO_2 separation [19]. Many studies have shown that embedding functional groups (such as -F, -NO_2, -NH_2, -OH) into MOF channels can also improve the separation selectivity of C_2H_2/C_2H_4 without a slight sacrifice in intrinsic moderate pore volumes or surface areas to adsorb a large amount of the objective gas molecules [20,21]. Therefore, if a porous MOF contains a suitable pore system that is simultaneously provided with both moderate pore size and high-density accessible functional groups like HBAs, it may synchronously possess satisfactory separation performance for C_2H_2/CO_2 and C_2H_2/C_2H_4 mixtures. Although multiple design strategies, such as the isoreticular chemistry principle [22], pore–space partition strategy [23], and forming structural interpenetration [24], have been developed to guide the synthesis of desired MOF materials, difficult challenges still remain in customizing MOF materials with desirable pore systems. This is because even subtle effects can lead to undesirable results in the uncontrollable and complex self-assembly process of the MOFs.

Herein, we designed and synthesized a novel Ni-MOF $\{[Ni(TPT)(NPC)(H_2O)]\cdot solvent\}_n$ (**NUM-14**, TPT = 2,4,6-tri(4-pyridinyl)-1,3,5-triazine, H_2NPC = 3-nitrophthalic acid), fea-

turing a desired pore size of 5.8 Å and functionalized pore environment decorated by abundant nitro groups serving as hydrogen bond receptors, which can preferentially capture C_2H_2 for achieving efficient separation of C_2H_2/CO_2 and C_2H_2/C_2H_4 mixtures. The single-component adsorption isotherms indicate that **NUM-14a** (activated **NUM-14**) has a good adsorption capacity for C_2H_2 with 4.44 mmol g^{-1}, exceeding some cutting-edge MOF materials. The predicted IAST selectivities and practical breakthrough experiments for C_2H_2/C_2H_4 and C_2H_2/CO_2 mixtures demonstrated that **NUM-14a** has favourable separation potential for these two kinds of mixed gases. Moreover, the values of Q_{st} calculation quantitatively vindicated that **NUM-14a** owns the strongest interaction with C_2H_2, stronger than with CO_2 and C_2H_4, which is also proved from another side by Grand Canonical Monte Carlo (GCMC) calculations. Both experimental and theoretical results show that **NUM-14a** can realize the efficient separation of C_2H_2 from CO_2 and C_2H_4, and that this fine performance mainly comes from its suitable pore system.

2. Results and Discussion

2.1. Single Crystal X-ray Diffraction Structure

The solvothermal reaction of TPT, H_2NPC, and $Ni(NO_3)_2$ in a DMF/H_2O mixed solvent system at 100 °C for 72 h harvested jade-green blocky crystals of as-synthesized **NUM-14**. The crystallographic structure analysis manifested that **NUM-14** crystallizes in the trigonal $P3_121$ space group. The asymmetric unit of **NUM-14** contains one Ni^{2+} atom, half of deprotonated NPC^{2-} ligand, and a half of TPT ligand. Each Ni^{2+} atom has a six-coordinate mode to form slightly distorted octahedral geometry with three N atoms from three different TPT ligands and two carboxylate O atoms from two different NPC^{2-} linkers, as well as one terminal water molecule. Each NPC^{2-} ligand connected two Ni^{2+} atoms to form a 1D infinite helix chain spiraling counterclockwise along the c axis. Each TPT ligand also coordinate with two Ni^{2+} atoms to generate two kinds of infinite 1D helix chains along the c axis, in which one of them rotates clockwise and another inversely rotates counterclockwise (Figure S1). Then three types of spiral chains make up one channel column. The remaining end of TPT ligands as pore wall on each channel column is connected to the adjacent channel column to form two kinds of one-dimensional channel structures along the c axis, one of which is the triangular channel with an aperture of about 6 Å while the another is similar to the former except that the nitro groups on the NPC^{2-} linkers toward its interior (Figure 1b–d). The coordinate mononuclear Ni^{2+} octahedron and TPT ligand can be simplified as 5- and 3-connected nodes, respectively (Figure 1a). Therefore, **NUM-14** can be simplified as a 2-nodal 3,5-connected topology network with the point symbol of $(4{\cdot}7^2)(4^3{\cdot}6^2{\cdot}7^4{\cdot}8)$ (Figure 1b) [25]. Calculation by *PLATON* revealed that the solvent-accessible volume in fully desolvated **NUM-14** is 59.4%. The accessible channel surface in **NUM-14a** is mainly composed of the pyridine/triazine rings and abundant nitro groups in ligands, getting a very polar and rich hydrogen bond receptor pore environment.

2.2. Purity and Stabilities of NUM-14

The experimental and activated PXRD patterns are strongly consistent with the simulated model based on the single-crystal data confirming the high-phase purity and skeleton stability after the degassing of **NUM-14** (Figure S2). The thermostability was demonstrated by TGA. As shown in Figure S3, it can be seen that the skeleton of **NUM-14** remains stable up to 300 °C. As shown in Figure S4, through testing PXRD of **NUM-14** samples soaked in various common solvents for 1 week, we found that **NUM-14** acquits itself well in solvent stability under different conditions.

2.3. Gas Adsorption Properties of NUM-14a

The activated sample of **NUM-14a** was prepared by heating the CH_2Cl_2-exchanged sample under preset high vacuum conditions at 40 °C for the duration of 10 h. Then, the N_2 sorption isotherm was recorded at 77 K to characterize and evaluate the permanent

porosity of **NUM-14a**. As indicated in Figure 2a, it shows a reversible type-I adsorption curve with the saturated loading of 289.9 cm^3 g^{-1} and is akin to multitudinous typical microporous MOF materials [26,27]. According to the N_2 adsorption isotherm, the BET (Brunauer–Emmett–Teller) and Langmuir surface areas were calculated, which reached 1075.5 and 1194.2 m^2 g^{-1}, respectively. The Horvath–Kawazoe method was applied to calculate the pore size distribution and the result exhibited the main aperture concentrates upon 5.8 Å, which allows small gas molecules to pass through easily.

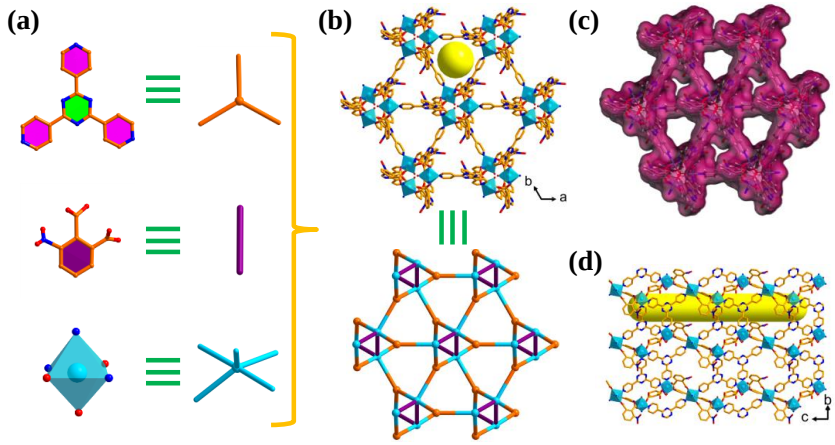

Figure 1. (**a**) Topology simplification of NiN_3O_3 octahedron and the ligands. (**b**) The triangular channel structure and topology simplification of 3D framework in **NUM-14** along the c axis. (**c**) The Connolly surface void spaces of **NUM-14**. (**d**) The side view of channel structure in **NUM-14** along the a-axis. Color code: Ni, sky blue; O, red; N, blue; C, light orange. Guest molecules and H atoms have been omitted for clarity.

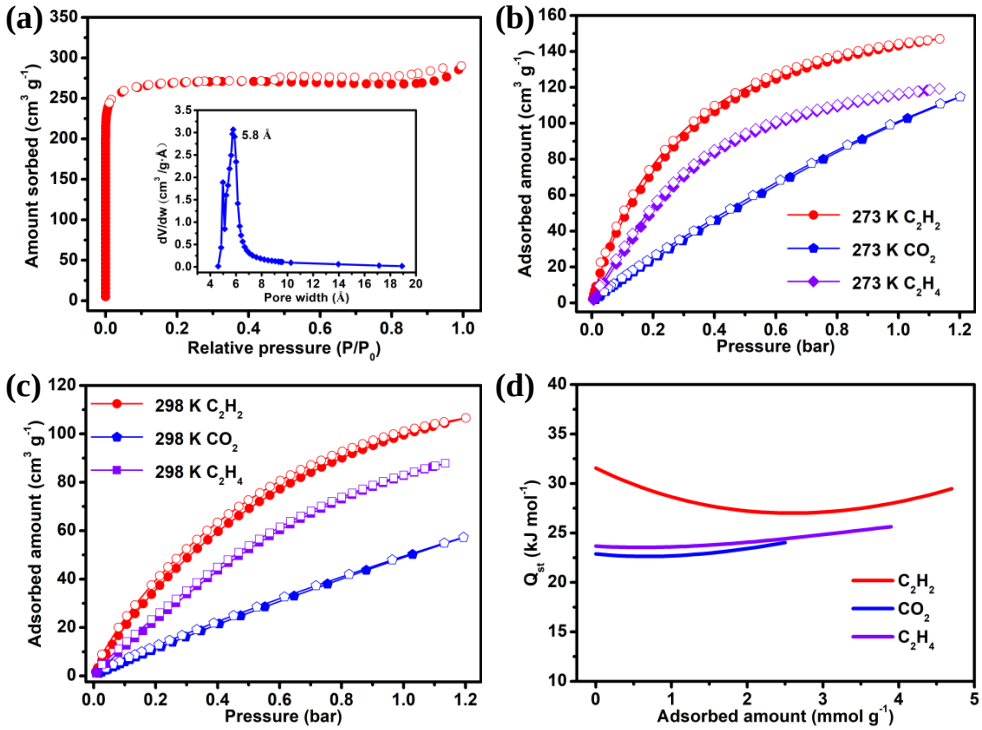

Figure 2. (**a**) N_2 sorption isotherm and pore size distribution of **NUM-14a** at 77 K. Single-component gas isotherms of C_2H_2, CO_2, and C_2H_4 for **NUM-14a** at (**b**) 273 K and (**c**) 298 K (filled and open symbols represent adsorption and desorption curves, respectively). (**d**) Isosteric enthalpy of adsorption of C_2H_2, CO_2, and C_2H in **NUM-14a**.

Combining with appropriate pore size and functionalized polar surface, **NUM-14a** is promising for evaluating C_2H_2 adsorption and separation performance from CO_2 and C_2H_4. As shown in Figure 2b,c, single-component sorption isotherms of **NUM-14a** for C_2H_2, CO_2, and C_2H_4 were measured at 273 and 298 K. Under 1 bar, these pure-component gas adsorption isotherms revealed that the C_2H_2 adsorption capacities of **NUM-14a** are 143.1 and 99.5 $cm^3\ g^{-1}$ at 273 and 298 K, respectively, which is markedly higher than that of CO_2 (102 and 50.2 $cm^3\ g^{-1}$) and C_2H_4 (115.8 and 82.7 $cm^3\ g^{-1}$), implying the distinctly stronger adsorption ability of **NUM-14a** for C_2H_2 than CO_2 and C_2H_4. Noteworthily, the adsorption capacity of C_2H_2 (4.44 mmol g^{-1}) at 298 K and 1 bar in **NUM-14a** is superior to most top-performing MOFs, like Zn-FBA (1.03 mmol g^{-1}) [28], IPM-101 (2.55 mmol g^{-1}) [29], ZNU-1 (3.41 mmol g^{-1}) [30], ZNU-4 (3.58 mmol g^{-1}) [31], and ZJU-74a (3.83 mmol g^{-1}) [32], which is attributed to its high porosity. Moreover, the C_2H_2/CO_2 uptake ratio at 298 K and 1 bar for **NUM-14a** reaches 1.98, while the uptake ratio of C_2H_2/C_2H_4 is only 1.20. Inspired by the distinctive uptake capacity and preferential binding of C_2H_2 for **NUM-14a**, we then calculated the isosteric enthalpies of adsorption (Q_{st}), a crucial metric that quantifies the interaction strength between gas molecules and pores in MOFs, by the Virial-type equation to quantitatively estimate the binding affinity between gas molecules and host framework (Figures S5–S7). The calculated Q_{st} at near-zero coverage for C_2H_2 (31.57 kJ mol^{-1}) is higher than CO_2 (22.89 kJ mol^{-1}) and C_2H_4 (23.67 kJ mol^{-1}), demonstrating the relatively stronger host–guest affinity for **NUM-14a** toward C_2H_2 in contrast to CO_2 and C_2H_4 (Figure 2d). These results of Q_{st} are adequately consistent with the gas adsorption behaviors as depicted in single-component isotherms and prove the feasibility of the C_2H_2 preferential adsorption in the framework of **NUM-14a**.

2.4. Gas Separation Performances of NUM-14a

Given the preferential capture and stronger affinity of C_2H_2 than CO_2 and C_2H_4 in **NUM-14a**, IAST was further adopted to evaluate the separation performances of **NUM-14a** for C_2H_2/CO_2 and C_2H_2/C_2H_4 mixtures. Single-component adsorption isotherms of C_2H_2 and C_2H_4 obtained from experimental determinations were fitted by the dual-site Langmuir–Freundlich model, while the isotherms of CO_2 were fitted by the single-site Langmuir–Freundlich equation for pursuing the more accurate consistency between experimental data and theoretical model (Figures S8–S13). The fitting results were then used to predictably calculate adsorptive selectivities for equimolar C_2H_2/CO_2 and C_2H_2/C_2H_4 with two different ratios of 50/50 or 1/99 at 273 and 298 K (Figure 3a,b). As revealed in Figure 3b, the calculated selectivity of **NUM-14a** for equimolar C_2H_2/CO_2 (50:50, v/v) is 3.37 at 298 K and 100 kPa, which is lower than some famous MOF materials under the same conditions, such as CuI@UiO-66-$(COOH)_2$ (185.00) [33], ATC-Cu (53.60) [34], and MOF-OH (25.00) [35], and slightly lower than that of FJU-118a (7.80) [36], BUT-85 (6.10) [37], but higher than many other well-known materials, such as [Ca(dtztp)$_{0.5}$] (1.70) [38], [Ni(tzba)$_{0.5}$(F)(bpy)] (2.20) [39], CAU-10H (2.50) [40] and SNNU-5-Sc (2.66) [41]. Due to the similar C_2H_2 and C_2H_4 adsorption behavior, although **NUM-14a** exhibits relatively low selectivities for C_2H_2/C_2H_4 mixtures with volume ratios of 1:99 (1.63) and 50:50 (1.61) at 298 K and 100 kPa, the result for C_2H_2/C_2H_4 (1:99, v/v) is still comparable to many consequences of reported MOFs, such as 1.13 for NUM-12a [42], 1.61 for Zn(ad)(int) [4], 1.59 for ZJNU-14 [43], 1.77 for ZJNU-7 [44], and 2.1 for UiO-67-$(NH_2)_2$ (Table S2) [45].

To further evaluate the separation performance of **NUM-14a** for C_2H_2/CO_2 and C_2H_2/C_2H_4 mixtures, we performed dynamic breakthrough experiments in a packed tube using **NUM-14a** as physical adsorbent at 298 K under a total inlet gas flow rate of 2 mL min^{-1}. As shown in Figure 4a, the breakthrough curve clearly proves that **NUM-14a** can effectively separate the C_2H_2/CO_2 mixture. When the equimolar C_2H_2/CO_2 gas mixture passes through the adsorption column, the CO_2 gas first elutes due to its deficient uptake capacity. Then, C_2H_2 breaks through the packed column with a penetration time of 19 min g^{-1} and the adsorbent slowly tends to saturate soon afterward. Ultimately, the outlet gas flow reaches adsorption equilibrium with the same components as the imported

stream at 55 min g^{-1}. Similarly, the separation performance of **NUM-14a** for the equimolar C_2H_2/C_2H_4 mixture is described in Figure 4b. The experiment result displays that C_2H_2 gas can be more preferably adsorbed in the separation unit than C_2H_4, so the pure C_2H_4 can be obtained with a time interval of 5 min g^{-1}, which is shorter than the breakthrough time of the C_2H_2/CO_2 mixture because of the stronger adsorption capacity of C_2H_4 relative to CO_2. These breakthrough tests undoubtedly testify to the ability of **NUM-14a** for separating C_2H_4 from mixtures containing CO_2 or C_2H_4.

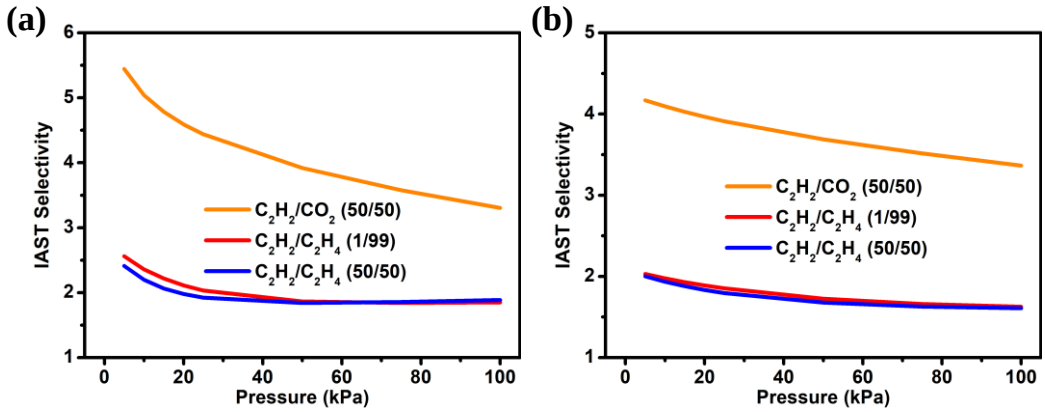

Figure 3. (**a**) The adsorption selectivities of **NUM-14a**, predicted from IAST for C_2H_2/CO_2 (50:50, v/v), C_2H_2/C_2H_4 (1:99, v/v) and C_2H_2/C_2H_4 (50:50, v/v) at 273 K (**a**) and 298 K (**b**).

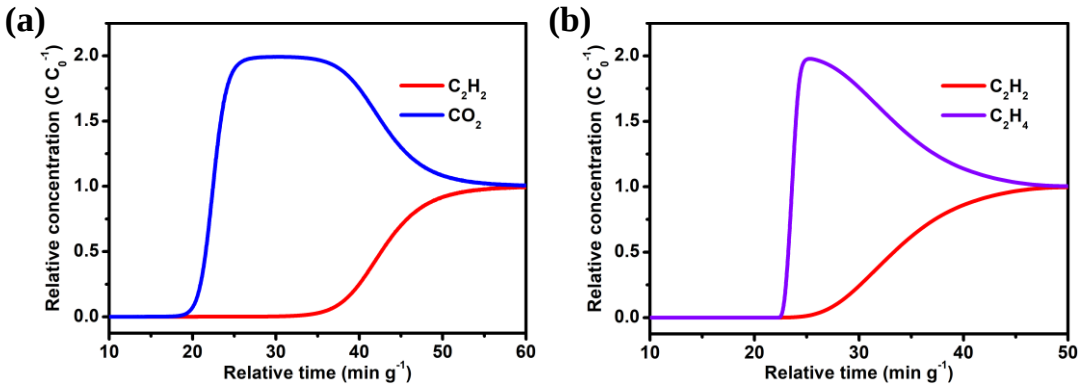

Figure 4. The column breakthrough curves for mixture gases of (**a**) C_2H_2/CO_2 (50:50, v/v), and (**b**) C_2H_2/C_2H_4 (50:50, v/v). The experiments were conducted at 298 K and the inlet gas flow rate was maintained at 2 mL min^{-1}.

2.5. Adsorption Mechanism

To profoundly investigate the interesting gas adsorption behaviors between the preferential sites and adsorbed gas molecules within **NUM-14a**, GCMC calculations were conducted to probe the interaction between the gas molecules and the host framework at 298 K and 1 bar. As shown in Figure 5a, for adsorbed C_2H_2 in pores, three strong binding sites of hydrogen bonds were found, where two distances of C-H···O between C_2H_2 and two nitro oxygen atoms are 2.378 Å and 3.608 Å, and the distance of C-H···O between terminal hydrogen atom of C_2H_2 and one carbonyl oxygen atom is 2.611 Å. The CO_2 molecule only interacts with the framework of **NUM-14a** through one weak C-H···O (3.562 Å) hydrogen bond interaction between acidic hydrogen atom on the pyridine ring and the basic oxygen atom at the end of CO_2 molecule (Figure 5b). For the C_2H_4 molecule which has weaker acidic than C_2H_2 and therefore has a weaker affinity to basic sites, two hydrogen bond interactions between C_2H_4 with two nitroxides were sought with long C-H···O distances (2.487 and 3.074 Å) (Figure 5c). By comparing GCMC calculation results, we can find that the pore surface of **NUM-14a** shows a stronger recognition effect on

C_2H_2 molecules than CO_2 and C_2H_4, explaining the reason for outstanding capture and separation performance of C_2H_2 in **NUM-14a** observed in experiments.

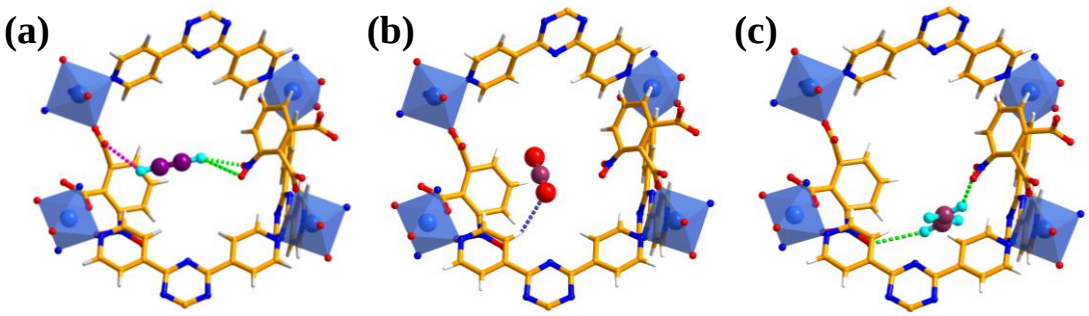

Figure 5. The GCMC calculated adsorption sites of C_2H_2 (**a**), CO_2 (**b**), and C_2H_4 (**c**) in **NUM-14a** at 298 K and 1 bar.

According to the adsorption data, we can find that **NUM-14a** has a good adsorption capacity for C_2H_2, which is mainly attributed to its medium pore size and large porosity. Moreover, the combination of separation experiments and the simulation calculations shows that **NUM-14a** has stronger binding forces for C_2H_2 compared with CO_2 and C_2H_4, which is possibly ascribed to the stronger synergistic hydrogen bond interactions between C_2H_2 and nitro group and the exposed oxygen atom. All of these prove that the customized fabrication of a pore system with moderate pore size and modified surface with HBAs in MOFs is beneficial to separate C_2H_2/CO_2 and C_2H_2/C_2H_4 mixtures.

3. Materials and Methods

3.1. Materials and Characterization

All chemicals and reagents were purchased from commercial suppliers and used without further purification. Powder X-ray diffraction (PXRD) was measured on a Rigaku Miniflex 600 with Cu Kα radiation (λ = 1.5425 Å) under air conditions. Thermogravimetric analysis (TGA) was recorded on a Rigaku standard thermogravimetry-differential thermal analysis (TG-DTA) analyzer, utilizing an empty and clean Al_2O_3 crucible as reference (heating rate = 10 °C min^{-1} in Ar atmosphere).

3.2. Gas Sorption Measurements

Before the sorption measurement, the sample of **NUM-14** was soaked in dichloromethane for 3 days to exchange solvent molecules in the channels. The degas procedure for the solvent-exchanged **NUM-14** was conducted at 40 °C under a high vacuum (less than 10^{-5} Torr) for 10 h and led to the formation of activated sample **NUM-14a**. The N_2 sorption isotherm measurement was carried out using a Micrometrics ASAP 2460 volumetric gas adsorption analyzer at 77 K in a liquid nitrogen bath. The C_2H_2, C_2H_4, and CO_2 sorption isotherm measurements were carried out at 273 and 298 K respectively using a Micrometrics ASAP 2020M volumetric gas adsorption analyzer.

3.3. X-ray Crystallography

Single-crystal X-ray diffraction data of **NUM-14** were collected on the Rigaku XtaLAB PRO MM007 DW diffractometer with Cu Kα radiation (λ = 1.54184 Å) at T = 99.99 (1) K. The structure was solved with the *SHELXT* program and refined by full-matrix least-squares against F^2 using the *SHELXL* program [46,47]. Anisotropic thermal parameters were implemented to all non-hydrogen atoms, and all hydrogen atoms were placed in the calculated positions and refined with isotropic thermal parameters. The *Solvent Mask* in *Olex2* software was employed to remove scattering contributions of the disordered solvent molecules and the generated solvent-free data of direction intensities were further refined [48]. Details of the crystal parameters, data collection, and refinement of **NUM-14** are listed in Table S1.

3.4. Synthesis of NUM-14

A solvothermal reaction of $Ni(NO_3)_2 \cdot 6H_2O$ (29.0 mg, 0.1 mmol), TPT (18.7 mg, 0.06 mmol), and H_2NPC (21.1 mg, 0.1 mmol) in 2.5 mL of a mixed solvent of DMF/H_2O (4:1, *v*/*v*) was kept at 100 °C for 3 days, and blocky crystals of **NUM-14** were first time synthesized in 83% yield based on the TPT ligand. When the reaction temperature slowly cooled to room temperature, a fresh sample was collected by filtration and washed with fresh DMF several times.

3.5. Isosteric Enthalpy of Adsorption Calculations

The experimental adsorption data of C_2H_2, CO_2, and C_2H_4 at 273 and 298 K in **NUM-14a** were fitted using a virial model (Equation (1)):

$$\boldsymbol{lnP} = \boldsymbol{lnN} + \frac{\mathbf{1}}{\boldsymbol{T}}\sum_{\boldsymbol{i}=\mathbf{0}}^{\boldsymbol{m}} \boldsymbol{a_i N^i} + \sum_{\boldsymbol{j}=\mathbf{0}}^{\boldsymbol{n}} \boldsymbol{b_j N^j} \quad (1)$$

where $\boldsymbol{P}$ is the pressure in Torr, $\boldsymbol{N}$ is the adsorbed amount in mmol g^{-1}, $\boldsymbol{T}$ is the temperature in K, and $\boldsymbol{a_i}$ and $\boldsymbol{b_j}$ are virial coefficients.

The isosteric enthalpies of adsorption ($\boldsymbol{Q_{st}}$) were calculated based on the fitted virial coefficients using the following equation (Equation (2)):

$$\boldsymbol{Q_{st}} = -\boldsymbol{R}\sum_{\boldsymbol{i}=\mathbf{0}}^{\boldsymbol{m}} \boldsymbol{a_i N^i} \quad (2)$$

$\boldsymbol{Q_{st}}$ is the coverage-dependent isosteric heat of adsorption and $\boldsymbol{R}$ is the universal gas constant.

3.6. Adsorption Selectivity Calculations

Ideal adsorbed solution theory (IAST) was utilized to predict gas adsorption selectivity of binary mixtures from the experimental single-component isotherms of C_2H_2, CO_2, and C_2H_4 [49]. The experimental pure-component adsorption isotherms of C_2H_2 and C_2H_4 were initially fitted by the dual-site Langmuir–Freundlich model (Equation (3)), while CO_2 was fitted by the single-site Langmuir–Freundlich model. That is, only the first half of Equation (3) is used to fit the experimental data to obtain a perfect fitting degree:

$$\boldsymbol{q} = \frac{\boldsymbol{q_{A,sat}} \boldsymbol{b_A} \boldsymbol{p}^{\mathbf{1}/\boldsymbol{n_1}}}{\mathbf{1} + \boldsymbol{b_A} \boldsymbol{p}^{\mathbf{1}/\boldsymbol{n_1}}} + \frac{\boldsymbol{q_{B,sat}} \boldsymbol{b_A} \boldsymbol{p}^{\mathbf{1}/\boldsymbol{n_2}}}{\mathbf{1} + \boldsymbol{b_B} \boldsymbol{p}^{\mathbf{1}/\boldsymbol{n_2}}} \quad (3)$$

where $\boldsymbol{p}$ is the pressure in kPa, $\boldsymbol{q}$ is the adsorbed amount in mmol g^{-1}, and $\boldsymbol{q_{A,sat}}$ and $\boldsymbol{q_{B,sat}}$ are the saturation capacities of two distinct adsorption sites $\boldsymbol{A}$ and $\boldsymbol{B}$ in mmol g^{-1}. $\boldsymbol{b_A}$ and $\boldsymbol{b_B}$ are the affinity coefficients in kPa^{-1}, and $\boldsymbol{n_1}$ and $\boldsymbol{n_2}$ represent the deviations from an ideal homogeneous surface.

Then the fitted parameters were used to calculate the selectivity (Equation (4)):

$$\boldsymbol{S_{A/B}} = \frac{\boldsymbol{X_A}/\boldsymbol{X_B}}{\boldsymbol{Y_A}/\boldsymbol{Y_B}} \quad (4)$$

In which, $\boldsymbol{X_i}$ and $\boldsymbol{Y_i}$ represent the mole fractions of component $\boldsymbol{i}$ in the adsorbed and bulk phases, respectively.

3.7. Breakthrough Experiments

The breakthrough experiments for C_2H_2/CO_2 (50:50, *v*/*v*) and C_2H_2/C_2H_4 (50:50, *v*/*v*) mixtures were completed on the Multi-component Adsorption Breakthrough Curve Analyzer from Beishide Instrument Technology Co., Ltd. (Beijing, China). An activated crystalline powder sample (1.30 g) was packed into a breakthrough column (6 mm diameter and 4 mL volume) with a 3 cm length of the sample loading, which was purged with He

flow (50 mL min^{-1}), sustaining 120 min at 40 °C before each breakthrough experiment. Subsequently, the mixed gas flows of C_2H_2/CO_2 and C_2H_2/C_2H_4 with a flow rate of 2 mL min^{-1} were respectively introduced into the adsorber at 298 K. At the same time, the compositions of effluents from the packed column were monitored and analyzed in real-time by online mass spectrometry.

3.8. Grand Canonical Monte Carlo Simulations

The GCMC simulations were performed for the adsorption of C_2H_2, CO_2, and C_2H_4 in **NUM-14a** with the Material Studio 8.0. The optimal adsorption sites were simulated under 298 K with a pressure of 1.0 bar. We used 1.0×10^7 cycles for equilibration, and the production steps were set to 1.0×10^6. The framework of **NUM-14a** and adsorbate molecules were treated as a rigid structure. A standard Lennard–Jones and Coulomb model was used and the Lennard–Jones parameters for the framework atoms as well as adsorbate molecules were adopted from the universal force field (UFF). Ewald summation was used to calculate electrostatic interactions for both adsorbent–adsorbate and adsorbateadsorbate interactions.

4. Conclusions

In summary, we constructed a new Ni-based MOF **NUM-14**, which has a fascinating pore system featuring an appropriate pore size and pleasant pore environment, to separate C_2H_2 well from CO_2 and C_2H_4. By a feat of its pore characteristic, **NUM-14a** can adsorb more C_2H_2 than CO_2 and C_2H_4. With the advantages of a nitro-functionalized pore wall framework, **NUM-14a** expresses greater affinity to C_2H_2 through hydrogen bond interactions. Furthermore, the strong pure-component gas adsorption behavior and favorable C_2H_2/CO_2, and C_2H_2/C_2H_4 separation performance are achieved by **NUM-14a**. In addition, the underlying selective adsorption mechanism and separation reason are revealed by GCMC simulations at the molecular level. This work can guide the designed synthesis of desirable MOFs with a tailor-made pore system and practical application of them for high-challenge gas separation problems.

Supplementary Materials: The following supporting information can be downloaded at: https://www.mdpi.com/article/10.3390/molecules27185929/s1. Table S1. Crystal data and structure refinement parameters for **NUM-14**. Table S2. Comparisons of C_2H_2 uptake and selectivities of C_2H_2/CO_2 and C_2H_2/C_2H_4 for **NUM-14a** and other MOFs. Figure S1. Three kinds of helix chains constitute the channel column of **NUM-14**. Figure S2. Comparison of simulated, experimental, and activated PXRD patterns of **NUM-14**. Figure S3. TGA curve for **NUM-14** under Ar atmosphere. Figure S4. The PXRD patterns for **NUM-14** after immersed in common solvents a week. Figures S5–S7. The details of Virial equation fitting to the experimental C_2H_2, CO_2, and C_2H_4 adsorption data for **NUM-14a**. Figures S8–S13. The details of dual/single-site Langmuir–Freundlich isotherm fitting to the experimental C_2H_2, CO_2, and C_2H_4 adsorption data for **NUM-14a** at 273 and 298 K. Figures S14–S16. Density distributions of C_2H_2, CO_2, and C_2H_4 in **NUM-14a** at 298 K and 1 bar.

Author Contributions: Q.Z.: Conceptualization, Methodology, Visualization, Investigation, Writing-original draft. G.-N.H.: Investigation. X.L.: Software, Formal analysis. S.-Q.Y.: Investigation. T.-L.H.: Supervision, Conceptualization, Writing—review & editing, Project administration, Funding acquisition. All authors have read and agreed to the published version of the manuscript.

Funding: The authors acknowledge the Natural Science Foundation of Tianjin (20JCYBJC01330), and the National Natural Science Foundation of China (21673120) for financial support of this work.

Institutional Review Board Statement: Not applicable.

Informed Consent Statement: Not applicable.

Data Availability Statement: The data that support the findings of this study are available in the Supplementary Materials of this article or from the corresponding author upon reasonable request.

Conflicts of Interest: There are no conflicts to declare.

Sample Availability: Samples of the compound **NUM-14** are available from the authors.

References

1. Sholl, D.S.; Lively, R.P. Seven chemical separations to change the world. *Nature* **2016**, *532*, 435–437. [CrossRef] [PubMed]
2. Pässler, P.; Hefner, W.; Buckl, K.; Meinass, H.; Meiswinkel, A.; Wernicke, H.-J.; Ebersberg, G.; Müller, R.; Bässler, J.; Behringer, H.; et al. *Ullmann's Encyclopedia of Industrial Chemistry*; Wiley-VCH: Weinheim, Germany, 2000.
3. Yang, S.-Q.; Hu, T.-L. Reverse-selective metal-organic framework materials for the efficient separation and purification of light hydrocarbons. *Coord. Chem. Rev.* **2022**, *468*, 214628. [CrossRef]
4. Ding, Q.; Zhang, Z.; Liu, Y.; Chai, K.; Krishna, R.; Zhang, S. One-step ethylene purification from ternary mixtures in a metal-organic framework with customized pore chemistry and shape. *Angew. Chem. Int. Ed.* **2022**, *61*, e202208134. [CrossRef] [PubMed]
5. Yang, S.-Q.; Sun, F.-Z.; Liu, P.; Li, L.; Krishna, R.; Zhang, Y.-H.; Li, Q.; Zhou, L.; Hu, T.-L. Efficient purification of ethylene from C2 hydrocarbons with an C_2H_6/C_2H_2-selective metal-organic framework. *ACS Appl. Mater. Interfaces* **2021**, *13*, 962–969. [CrossRef] [PubMed]
6. Chen, Y.; Xiong, Q.; Wang, Y.; Du, Y.; Wang, Y.; Yang, J.; Li, L.; Li, J. Boosting molecular recognition of acetylene in UiO-66 framework through pore environment functionalization. *Chem. Eng. Sci.* **2021**, *237*, 116572. [CrossRef]
7. Mu, X.-B.; Xue, Y.-Y.; Hu, M.-C.; Zhang, P.; Wang, Y.; Li, H.-P.; Li, S.-N.; Zhai, Q.-G. Fine-tuning of pore-space-partitioned metal-organic frameworks for efficient C_2H_2/C_2H_4 and C_2H_2/CO_2 separation. *Chin. Chem. Lett.* **2022**. [CrossRef]
8. Zhang, Q.; Zhou, L.; Liu, P.; Li, L.; Yang, S.-Q.; Li, Z.-F.; Hu, T.-L. Integrating tri-mural nanotraps into a microporous metal-organic framework for C_2H_2/CO_2 and C_2H_2/C_2H_4 separation. *Sep. Purif. Technol.* **2022**, *296*, 121404. [CrossRef]
9. Sahoo, R.; Das, M.C. C2s/C1 hydrocarbon separation: The major step towards natural gas purification by metal-organic frameworks (MOFs). *Coord. Chem. Rev.* **2021**, *442*, 213998. [CrossRef]
10. Shao, Y.-R.; Zhou, L.; Yu, L.; Li, Z.-F.; Li, Y.-T.; Li, W.; Hu, T.-L. In situ construction of a Co/ZnO@C heterojunction catalyst for efficient hydrogenation of biomass derivative under mild conditions. *ACS Appl. Mater. Interfaces* **2022**, *14*, 17195–17207. [CrossRef]
11. Pal, S.C.; Das, M.C. Superprotonic conductivity of MOFs and other crystalline platforms beyond 10^{-1} S cm^{-1}. *Adv. Funct. Mater.* **2021**, *31*, 2101584. [CrossRef]
12. Xu, Y.; Yang, S.-L.; Li, G.; Bu, R.; Liu, X.-Y.; Gao, E.-Q. Cooperative protonation underlying the acid response of metal-organic frameworks. *Chem. Mater.* **2022**, *34*, 5500–5510. [CrossRef]
13. Qazvini, O.T.; Babarao, R.; Telfer, S.G. Multipurpose metal-organic framework for the adsorption of acetylene: Ethylene purification and carbon dioxide removal. *Chem. Mater.* **2019**, *31*, 4919–4926. [CrossRef]
14. Verma, G.; Ren, J.; Kumar, S.; Ma, S. New paradigms in porous framework materials for acetylene storage and separation. *Eur. J. Inorg. Chem.* **2021**, *44*, 4498–4507. [CrossRef]
15. Luna-Triguero, A.; Vicent-Luna, J.M.; Madero-Castro, R.M.; Gómez-Álvarez, P.; Calero, S. Acetylene storage and separation using metal-organic frameworks with open metal sites. *ACS Appl. Mater. Interfaces* **2019**, *11*, 31499–31507. [CrossRef]
16. Wen, H.-M.; Wang, H.; Li, B.; Cui, Y.; Wang, H.; Qian, G.; Chen, B. A microporous metal-organic framework with lewis basic nitrogen sites for high C_2H_2 storage and significantly enhanced C_2H_2/CO_2 separation at ambient conditions. *Inorg. Chem.* **2016**, *55*, 7214–7218. [CrossRef]
17. Yang, L.; Jin, A.; Ge, L.; Cui, X.; Xing, H. A novel interpenetrated anion-pillared porous material with high water tolerance afforded efficient C_2H_2/C_2H_4 separation. *Chem. Commun.* **2019**, *55*, 5001–5004. [CrossRef]
18. Cui, X.; Chen, K.; Xing, H.; Yang, Q.; Krishna, R.; Bao, Z.; Wu, H.; Zhou, W.; Dong, X.; Han, Y.; et al. Pore chemistry and size control in hybrid porous materials for acetylene capture from ethylene. *Science* **2016**, *353*, 141–144. [CrossRef]
19. Xue, Y.-Y.; Bai, X.-Y.; Zhang, J.; Wang, Y.; Li, S.-N.; Jiang, Y.-C.; Hu, M.-C.; Zhai, Q.-G. Precise pore space partitions combined with high-density hydrogen-bonding acceptors within metal-organic frameworks for highly efficient acetylene storage and separation. *Angew. Chem. Int. Ed.* **2021**, *60*, 10122–10128. [CrossRef]
20. Chen, F.; Bai, D.; Wang, X.; He, Y. A comparative study of the effect of functional groups on C_2H_2 adsorption in NbO-type metal-organic frameworks. *Inorg. Chem. Front.* **2017**, *4*, 960–967. [CrossRef]
21. Qazvini, O.T.; Macreadie, L.K.; Telfer, S.G. Effect of ligand functionalization on the separation of small hydrocarbons and CO_2 by a series of MUF-15 analogues. *Chem. Mater.* **2020**, *32*, 6744–6752. [CrossRef]
22. Fan, W.; Zhang, X.; Kang, Z.; Liu, X.; Sun, D. Isoreticular chemistry within metal-organic frameworks for gas storage and separation. *Coord. Chem. Rev.* **2021**, *443*, 213968. [CrossRef]
23. Hong, A.N.; Yang, H.; Bu, X.; Feng, P. Pore space partition of metal-organic frameworks for gas storage and separation. *EnergyChem* **2022**, *4*, 100080. [CrossRef]
24. Wang, T.; Lin, E.; Peng, Y.-L.; Chen, Y.; Cheng, P.; Zhang, Z. Rational design and synthesis of ultramicroporous metal-organic frameworks for gas separation. *Coord. Chem. Rev.* **2020**, *423*, 213485. [CrossRef]
25. Zhang, D.-S.; Chang, Z.; Li, Y.-F.; Jiang, Z.-Y.; Xuan, Z.-H.; Zhang, Y.-H.; Li, J.-R.; Chen, Q.; Hu, T.-L.; Bu, X.-H. Fluorous metal-organic frameworks with enhanced stability and high H_2/CO_2 storage capacities. *Sci. Rep.* **2013**, *3*, 3312.
26. Sun, F.-Z.; Yang, S.-Q.; Krishna, R.; Zhang, Y.-H.; Xia, Y.-P.; Hu, T.-L. Microporous metal-organic framework with a completely reversed adsorption relationship for C2 hydrocarbons at room temperature. *ACS Appl. Mater. Interfaces* **2020**, *12*, 6105–6111. [CrossRef] [PubMed]
27. Jiang, S.; Guo, L.; Chen, L.; Song, C.; Liu, B.; Yang, Q.; Zhang, Z.; Yang, Y.; Ren, Q.; Bao, Z. A strongly hydrophobic ethane-selective metal-organic framework for efficient ethane/ethylene separation. *Chem. Eng. J.* **2022**, *442*, 136152. [CrossRef]

28. Yang, L.; Yan, L.; Niu, W.; Feng, Y.; Fu, Q.; Zhang, S.; Zhang, Y.; Li, L.; Gu, X.; Dai, P.; et al. Adsorption in reversed order of C2 hydrocarbons on an ultramicroporous fluorinated metal-organic framework. *Angew. Chem. Int. Ed.* **2022**, *61*, e202204046. [CrossRef]
29. Sharma, S.; Mukherjee, S.; Desai, A.V.; Vandichel, M.; Dam, G.K.; Jadhav, A.; Kociok-Köhn, G.; Zaworotko, M.J.; Ghosh, S.K. Efficient capture of trace acetylene by an ultramicroporous metal-organic framework with purine binding sites. *Chem. Mater.* **2021**, *33*, 5800–5808. [CrossRef]
30. Wang, L.; Sun, W.; Zhang, Y.; Xu, N.; Krishna, R.; Hu, J.; Jiang, Y.; He, Y.; Xing, H. Interpenetration symmetry control within ultramicroporous robust boron cluster hybrid MOFs for benchmark purification of acetylene from carbon dioxide. *Angew. Chem. Int. Ed.* **2021**, *60*, 22865–22870. [CrossRef] [PubMed]
31. Xu, N.; Hu, J.; Wang, L.; Luo, D.; Sun, W.; Hu, Y.; Wang, D.; Cui, X.; Xing, H.; Zhang, Y. A TIFSIX pillared MOF with unprecedented zsd topology for efficient separation of acetylene from quaternary mixtures. *Chem. Eng. J.* **2022**, *450*, 138034. [CrossRef]
32. Pei, J.; Shao, K.; Wang, J.-X.; Wen, H.-M.; Yang, Y.; Cui, Y.; Krishna, R.; Li, B.; Qian, G. A chemically stable hofmann-type metal-organic framework with sandwich-like binding sites for benchmark acetylene capture. *Adv. Mater.* **2020**, *32*, 1908275. [CrossRef] [PubMed]
33. Zhang, L.; Jiang, K.; Yang, L.; Li, L.; Hu, E.; Yang, L.; Shao, K.; Xing, H.; Cui, Y.; Yang, Y.; et al. Benchmark C_2H_2/CO_2 separation in an ultra-microporous metal-organic framework via copper(I)-alkynyl chemistry. *Angew. Chem. Int. Ed.* **2021**, *60*, 15995–16002. [CrossRef]
34. Niu, Z.; Cui, X.; Pham, T.; Verma, G.; Lan, P.C.; Shan, C.; Xing, H.; Forrest, K.A.; Suepaul, S.; Space, B.; et al. A MOF-based ultra-strong acetylene nano-trap for highly efficient C_2H_2/CO_2 separation. *Angew. Chem. Int. Ed.* **2021**, *60*, 5283–5288. [CrossRef]
35. Gong, W.; Cui, H.; Xie, Y.; Li, Y.; Tang, X.; Liu, Y.; Cui, Y.; Chen, B. Efficient C_2H_2/CO_2 separation in ultramicroporous metal-organic frameworks with record C_2H_2 storage density. *J. Am. Chem. Soc.* **2021**, *143*, 14869–14876. [CrossRef]
36. Song, Q.; Yang, Y.; Yuan, F.; Zhu, S.; Wang, J.; Xiang, S.; Zhang, Z. Electrostatic force-driven lattice water bridging to stabilize a partially charged indium MOF for efficient separation of C_2H_2/CO_2 mixtures. *J. Mater. Chem. A* **2022**, *10*, 9363–9369. [CrossRef]
37. Si, G.-R.; Wu, W.; He, T.; Xu, Z.-C.; Wang, K.; Li, J.-R. Stable bimetallic metal-organic framework with dual-functional pyrazolate-carboxylate ligand: Rational construction and C_2H_2/CO_2 separation. *ACS Mater. Lett.* **2022**, *4*, 1032–1036. [CrossRef]
38. Wang, G.-D.; Li, Y.-Z.; Zhang, W.-F.; Hou, L.; Wang, Y.-Y.; Zhu, Z. Acetylene separation by a Ca-MOF containing accessible sites of open metal centers and organic groups. *ACS Appl. Mater. Interfaces* **2021**, *13*, 58862–58870. [CrossRef]
39. Wang, G.-D.; Wang, H.-H.; Shi, W.-J.; Hou, L.; Wang, Y.-Y.; Zhu, Z. A highly stable MOF with F and N accessible sites for efficient capture and separation of acetylene from ternary mixtures. *J. Mater. Chem. A* **2021**, *9*, 24495–24502. [CrossRef]
40. Ye, Y.; Xian, S.; Cui, H.; Tan, K.; Gong, L.; Liang, B.; Pham, T.; Pandey, H.; Krishna, R.; Lan, P.C.; et al. Metal-organic framework based hydrogen-bonding nanotrap for efficient acetylene storage and separation. *J. Am. Chem. Soc.* **2022**, *144*, 1681–1689. [CrossRef]
41. Lv, H.-J.; Zhang, J.-W.; Jiang, Y.-C.; Li, S.-N.; Hu, M.-C.; Zhai, Q.-G. Micropore regulation in ultrastable $[Sc_3O]$-organic frameworks for acetylene storage and purification. *Inorg. Chem.* **2022**, *61*, 3553–3562. [CrossRef]
42. Zhang, Q.; Yang, S.-Q.; Zhou, L.; Yu, L.; Li, Z.-F.; Zhai, Y.-J.; Hu, T.-L. Pore-space partition through an embedding metal-carboxylate chain-induced topology upgrade strategy for the separation of acetylene/ethylene. *Inorg. Chem.* **2021**, *60*, 19328–19335. [CrossRef]
43. Jiang, Z.; Fan, L.; Zhou, P.; Xu, T.; Chen, J.; Hu, S.; Chen, D.-L.; He, Y. An N-oxide-functionalized nanocage-based copper-tricarboxylate framework for the selective capture of C_2H_2. *Dalton Trans.* **2020**, *49*, 15672–15681. [CrossRef]
44. Jiang, Z.; Fan, L.; Zhou, P.; Xu, T.; Hu, S.; Chen, J.; Chen, D.-L.; He, Y. An aromatic-rich cage-based MOF with inorganic chloride ions decorating the pore surface displaying the preferential adsorption of C_2H_2 and C_2H_6 over C_2H_4. *Inorg. Chem. Front.* **2021**, *8*, 1243–1252. [CrossRef]
45. Gu, X.-W.; Wang, J.-X.; Wu, E.; Wu, H.; Zhou, W.; Qian, G.; Chen, B.; Li, B. Immobilization of lewis basic sites into a stable ethane-selective MOF enabling one-step separation of ethylene from a ternary mixture. *J. Am. Chem. Soc.* **2022**, *144*, 2614–2623. [CrossRef]
46. Sheldrick, G.M. *SHELXT*—Integrated space-group and crystal-structure determination. *Acta Cryst. A* **2015**, *71*, 3–8. [CrossRef]
47. Sheldrick, G.M. Crystal structure refinement with *SHELXL*. *Acta Cryst. C* **2015**, *71*, 3–8. [CrossRef]
48. Bourhis, L.J.; Dolomanov, O.V.; Gildea, R.J.; Howard, J.A.; Puschmann, H. The anatomy of a comprehensive constrained, restrained refinement program for the modern computing environment—*Olex2* dissected. *Acta Cryst. A* **2015**, *71*, 59–75. [CrossRef]
49. Myers, A.L.; Prausnitz, J.M. Thermodynamics of mixed-gas adsorption. *AlChE J.* **1965**, *11*, 121–127. [CrossRef]